eScience 2 (2022) 227–234

Contents lists available at ScienceDirect

eScience

journal homepage: www.keaipublishing.com/en/journals/escience

Research Paper

Large-scale synthesis of N-doped carbon capsules supporting atomically dispersed iron for efficient oxygen reduction reaction electrocatalysis

Hui Yang [b], Yanfang Liu [b], Xiaolu Liu [b], Xiangke Wang [b], He Tian [c], Geoffrey I.N. Waterhouse [d], Paul E. Kruger [e], Shane G. Telfer [f], Shengqian Ma [a,*]

[a] Department of Chemistry, University of North Texas, Denton, TX, 76201, United States
[b] College of Environmental Science and Engineering, North China Electric Power University, Beijing, 102206, PR China
[c] State Key Laboratory of Silicon Materials, Center of Electron Microscopy, School of Materials Science and Engineering, Zhejiang University, Hangzhou, 310027, PR China
[d] MacDiarmid Institute for Advanced Materials and Nanotechnology, School of Chemical Sciences, The University of Auckland, Auckland, 1142, New Zealand
[e] MacDiarmid Institute for Advanced Materials and Nanotechnology, School of Physical and Chemical Sciences, University of Canterbury, Christchurch, 8140, New Zealand
[f] MacDiarmid Institute for Advanced Materials and Nanotechnology, School of Fundamental Sciences, Massey University, Palmerston North, 4442, New Zealand

HIGHLIGHTS

- A hollow Fe-N_x-C was synthesized through ion exchange and pyrolysis.
- H-Fe-N_x-C could be synthesized on a large scale if required.
- H-Fe-N_x-C showed efficient electrocatalytic activity towards the ORR.

GRAPHICAL ABSTRACT

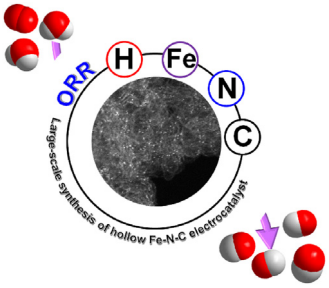

ARTICLE INFO

Keywords:
Metal single atoms
Hollow carbon capsules
Oxygen reduction reaction
Metal–organic framework
Electrocatalysis

ABSTRACT

The large-scale synthesis of platinum-free electrocatalysts for the oxygen reduction reaction (ORR) remains a grand challenge. We report the large-scale production of stable and active ORR electrocatalysts based on iron, an earth-abundant element. A core–shell zeolitic imidazolate framework–tannic acid coordination polymer composite (ZIF-8@K-TA) was utilized as the catalyst precursor, which was transformed into iron atoms dispersed in hollow porous nitrogen-doped carbon capsules (H-Fe-N_x-C) through ion exchange and pyrolysis. H-Fe-N_x-C features site-isolated single-atom iron centers coordinated to nitrogen in graphitic layers, high levels of nitrogen doping, and high permeability to incoming gases. Benefiting from these characteristics, H-Fe-N_x-C demonstrated efficient electrocatalytic activity ($E_{1/2}$ = 0.92 V, vs. RHE) and stability towards the ORR in both alkaline and acidic media. In ORR performance, it surpassed the majority of recently reported Fe-N-C catalysts and the standard Pt/C catalyst. In addition, H-Fe-N_x-C showed outstanding tolerance to methanol.

* Corresponding author.
E-mail address: shengqian.ma@unt.edu (S. Ma).

https://doi.org/10.1016/j.esci.2022.02.005
Received 3 October 2021; Received in revised form 5 January 2022; Accepted 21 February 2022
Available online 4 March 2022

1. Introduction

Rechargeable metal–air batteries and fuel cells are important technologies for a sustainable energy future [1–4]. Both devices use the oxygen reduction reaction (ORR) at the cathode for energy conversion [5–8]. Platinum and platinum alloys are generally considered the most active and stable catalysts for the electrocatalytic ORR [7–9]. However, the scarcity and high cost of platinum seriously limit the broad implementation of platinum-based catalysts in large-scale applications. To address this bottleneck, non-precious metal catalysts with efficiency and durability comparable to platinum's are being actively pursued. ORR catalysts now under serious evaluation include metal oxides [10–12], metal phosphides [13], nitrides and sulfides [14–16]. In addition, metal–nitrogen–carbon (M-N-C) catalysts are emerging as frontrunners in the development of new ORR catalysts, as discussed in detail below.

Over the past few years, metal single atoms anchored on porous nitrogen-doped carbon supports (denoted as M-N-C) [17,18], such as Fe-N-C [19–27], Co-N-C [28–31], Cu-N-C [32,33], and Mn-N-C [34–36], have been extensively explored as electrocatalysts for the ORR and other reactions. In many reactions, metal single-atom catalysts show remarkable catalytic activity and stability, which is explained by their highly accessible metal centers (M-N_x) being firmly embedded in conductive graphitic carbon layers. Doping graphitic carbon with nitrogen is crucial in generating sites for metal binding whilst also enhancing the hydrophilicity and electrical conductivity of the carbon support to promote efficient electrocatalysis [37,38]. In the absence of nitrogen binding sites, metals deposited on carbon supports simply aggregate to form nanoparticles. The synthesis of M-N-C catalysts with atomically dispersed metal sites typically employs high-temperature pyrolysis processes. However, unless care is taken to use suitable precursors, high-temperature pyrolysis generally leads to metal aggregation into nanoparticles, particularly during scale-up syntheses or when the metal content in the product is greater than a few atomic percent. This severely limits the practical application of M-N_x-C catalysts in the ORR. To allow the true potential of metal single-atom catalysts to be realized, versatile and scalable synthetic methods for M-N_x-C catalysts are needed that avoid metal sintering or aggregation.

Herein, we report the large-scale synthesis of Fe-N_x-C (denoted as H-Fe-N_x-C) catalysts, which are hollow and have well-defined nanostructural features such as an abundance of accessible M-N_x active sites and high porosity to allow efficient mass transport to the active sites. Our approach uses a core–shell precursor; the shell is essential to deliver hollow catalysts upon pyrolysis, rather than dense materials. H-Fe-N_x-C is an efficient ORR catalyst in both acidic and basic aqueous solutions, as evidenced by half-wave potentials of 0.92 V, which are 10 mV (0.1 M KOH) and 20 mV (0.1 M $HClO_4$) more positive than a state-of-art 20 wt% Pt/C catalyst and surpass the majority of reported M-N_x-C ORR catalysts. Further, H-Fe-N_x-C exhibits outstanding methanol tolerance and long-term durability and can be synthesized on a large scale (we fabricated 8.6 g in a single batch, which could easily be scaled up to 1 kg, if required), making it one of the best all-round M-N_x-C ORR catalysts reported to date.

2. Results

2.1. Large-scale synthesis of H-Fe-N_x-C and structural characterization

Synthesizing this well-defined H-Fe-N_x-C catalyst on a large scale would necessitate low-cost precursors and simple processing steps, so we used metal–organic framework (ZIF-8) nanocrystals coated by a tannic acid–metal coordination compound as a precursor to produce H-Fe-N_x-C. As shown in Fig. 1, ZIF-8 (50 g) nanocrystals were first prepared and coated with a tannic acid–potassium coordination compound to yield ZIF-8@K-TA core–shell nanocrystals (Step I). Post-synthetic cation exchange of the potassium ions in the K-TA shell by iron(III) yielded ZIF-8@Fe-TA core–shell nanocrystals (Step II in Fig. 1) [39–41]. Fourier transform infrared (FTIR) spectroscopy showed the appearance of -OH stretch (~3398 cm^{-1}) and C=O stretch (~1716 cm^{-1}) signals, which verified the successful coating of metal/tannic acid compound shells on the ZIF-8 surface (Fig. S1). Powder X-ray diffraction (PXRD) proved that the crystallinity of the ZIF core was maintained after the coating step, with the Fe-TA shell being amorphous (Figs. S2, S3, S12). After the Fe^{3+} exchange, the dodecahedral core–shell morphology was retained, as evidenced in Figs. S5–S11. Pyrolysis at 900 °C (Step III in Fig. 1), followed by acid treatment and a second pyrolysis step, transformed the ZIF-8@Fe-TA core–shell nanocrystals into N-doped carbon capsules with embedded FeN_x sites (H-Fe-N_x-C). During the pyrolysis step, Zn ions in the ZIF-8 core were reduced to metallic Zn atoms, which sublimed from the sample and were lost. The acid treatment acted to remove any residual Zn metal or Fe nanoparticles.

An array of experimental techniques supported the conclusion that the iron in the structure was atomically dispersed. Transmission electron

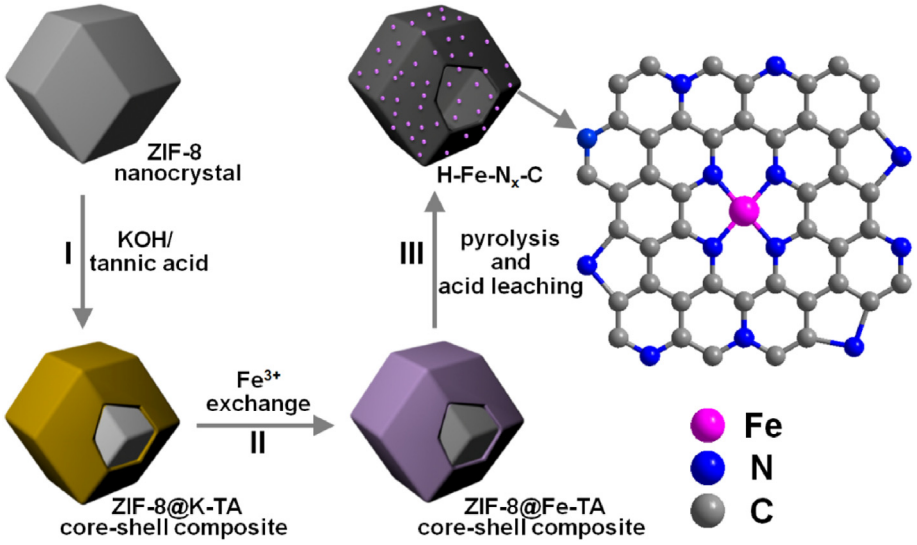

Fig. 1. Synthetic scheme for the preparation of H-Fe-N_x-C. Step I involves the deposition of a potassium–tannic acid coordination polymer on the surface of ZIF-8 nanocrystals. In Step II, the K^+ ions are exchanged for Fe^{3+}. Pyrolysis of this material at 900 °C (Step III), followed by acid leaching and a second pyrolysis step, generates H-Fe-N_x-C with atomically dispersed iron sites.

microscopy (TEM) and scanning electron microscopy (SEM) images showed that H-Fe-N_x-C had a hollow capsule-like structure, as was also observed for related reference materials (Figs. 2a and S13) [39–43]. No Fe nanoparticles were observed. We note that in the absence of the tannic acid shell layer, pyrolysis leads to a dense material [22]. Scanning transmission electron microscopy (STEM) and corresponding EDS (energy dispersive spectroscopy) mapping images showed a uniform distribution of the carbon, nitrogen, and iron in H-Fe-N_x-C (Figs. 2b–f). A large number of isolated spots against a dark background were clearly observed on the hollow carbon support using atomic-resolution HAADF-STEM (Fig. 2g, white spots). These spots corresponded to single iron atoms, which were well dispersed in the N-doped carbon support. As expected for Fe single atoms, the spots had an average width of about 1.5 Å, with ~93% of them measuring less than 2 Å in diameter.

The carbon components of the ZIF-8 and TA were completely converted to a graphite-rich form (or, more precisely, a N-doped graphite-rich form), as evidenced by the PXRD pattern and Raman spectroscopy (Figs. S4 and S16). The PXRD pattern of H-Fe-N_x-C showed diffraction peaks at 24° and 44°, which could readily be assigned to the (002) and (100) reflection planes of graphitic carbon, respectively (Fig. S4). Again, no evidence of Fe nanoparticles was seen. The relative areas of the D ($1350\ cm^{-1}$) and G ($1590\ cm^{-1}$) bands in Raman spectroscopy suggested that H-Fe-N_x-C contained significant graphite content, sufficient to offer good electrical conductivity (Fig. S16).

The yield of H-Fe-N_x-C was about 8.6 g (starting from 50 g of ZIF-8 nanocrystals), suggesting the synthesis method would potentially be straightforward to scale up (Fig. 2h) to produce kilograms of catalyst.

2.2. Coordination environment analysis of H-Fe-N_x-C

The H-Fe-N_x-C contained 6.26 wt% nitrogen and 0.74 wt% iron, as revealed by elemental analysis (EA) and inductively coupled plasma optical emission spectroscopy (ICP-OES), respectively (Table S1). X-ray photoelectron spectroscopy (XPS) was conducted to investigate the valence structure of H-Fe-N_x-C. The C 1s spectrum showed four major peaks with binding energies of 284.7, 285.8, 287.8, and 290.9 eV, corresponding to the sp^2/sp^3 C, C-N, C=O, and π-π^* signals, respectively (Fig. 3a). The Fe 2p XPS spectrum for H-Fe-N_x-C clearly showed signals that could be assigned to iron(II) and iron(III) (Fig. S17).

The doped form of nitrogen in the carbon capsules of H-Fe-N_x-C was probed by examining the N 1s XPS region (Fig. 3b). The spectrum was deconvoluted into peaks at 398.3, 399.9, 401.3, and 404.7 eV,

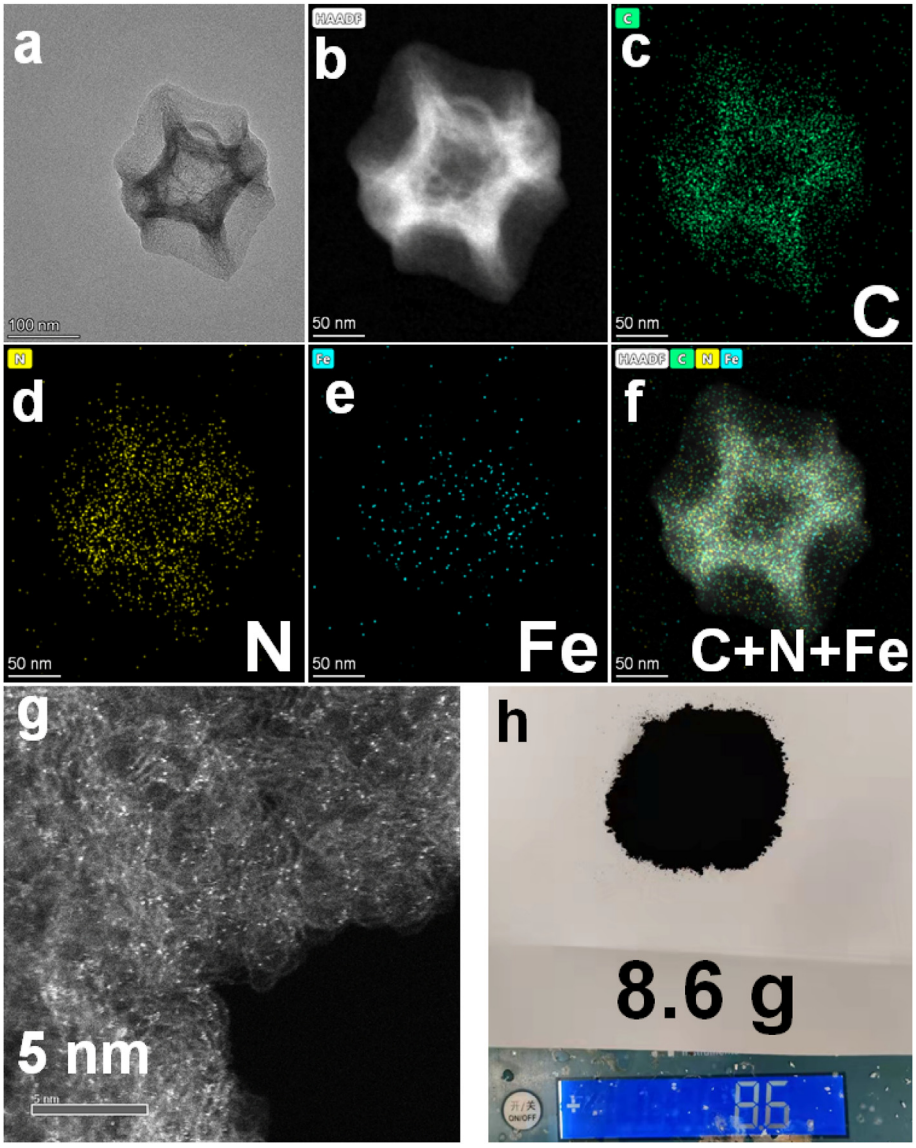

Fig. 2. Structural characterization. (a) TEM image of H-Fe-N_x-C. (b–f) HAADF-STEM image and corresponding element maps showing the distribution of carbon (green), nitrogen (yellow), and iron (cyan). (g) Atomic-resolution HAADF-STEM image of the H-Fe-N_x-C. (h) Photograph of the obtained H-Fe-N_x-C powder.

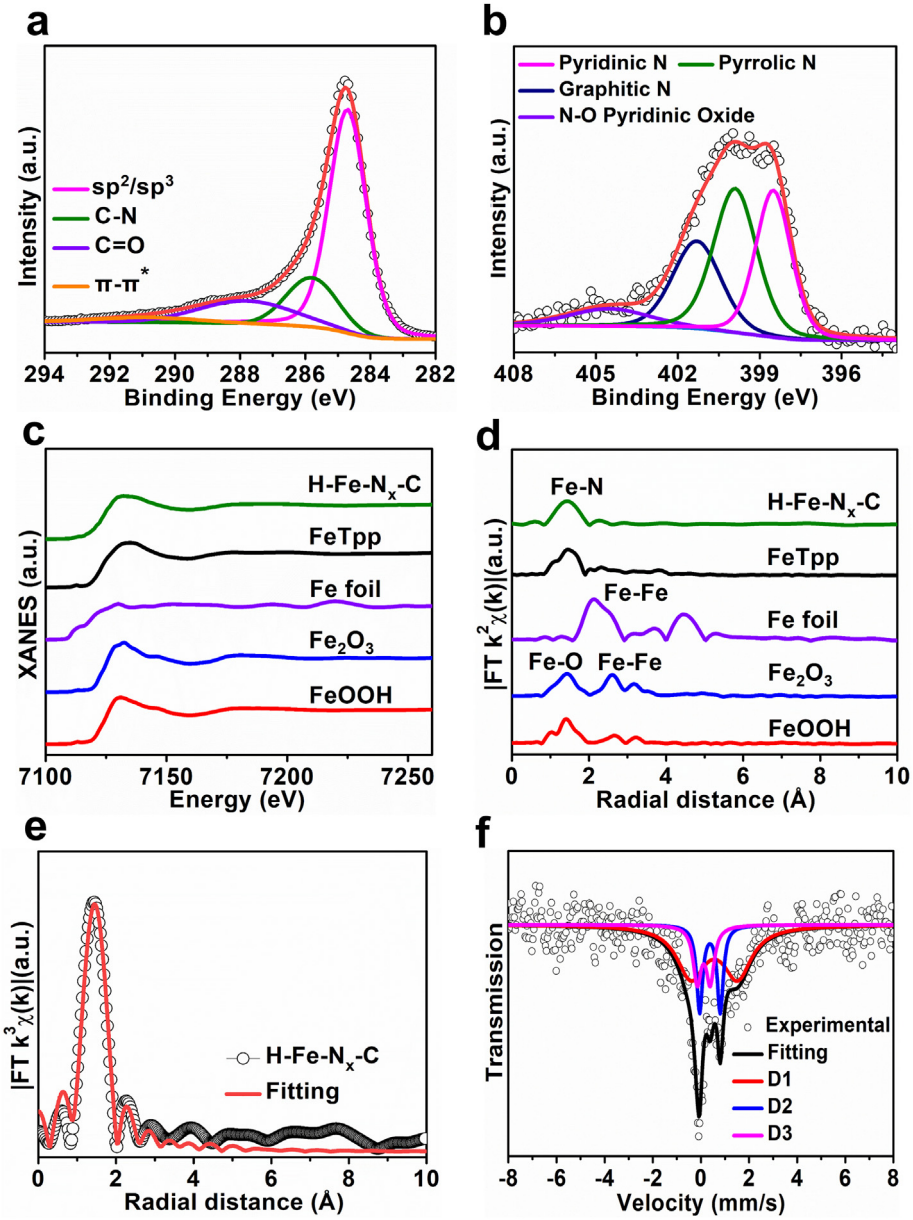

Fig. 3. Structural characterization. (**a**) C 1s XPS spectrum of H-Fe-N_x-C. (**b**) N 1s XPS spectrum of H-Fe-N_x-C. (**c**) Fe K-edge XANES spectra of H-Fe-N_x-C, together with various Fe standards. (**d**) Fe K-edge EXAFS spectra of H-Fe-N_x-C, together with various Fe standards. (**e**) Fitted EXAFS plots of H-Fe-N_x-C by Fe-N_4(C) scattering path in R space. (**f**) Fe Mössbauer transmission spectrum for H-Fe-N_x-C. The data for Fe foil, Fe_2O_3, FeOOH, and FeTpp in 3c and 3d were reported in our previous work [41].

corresponding to pyridinic N, pyrrolic N (and Fe-N_x), graphitic N, and N-O pyridinic oxide, respectively [27,44]. Fe-N_x sites are well known to promote the ORR, so their abundance in H-Fe-N_x-C was expected to be beneficial for electrocatalytic oxygen reduction.

Fe K-edge X-ray absorption spectroscopy was employed to examine the electronic structure and local coordination of iron sites in H-Fe-N_x-C. Fe-tetraphenylporphyrin (FeTpp), Fe_2O_3, Fe foil, and FeOOH were used as reference materials. The experimental X-ray absorption near edge structure (XANES) spectra in Fig. 3c revealed that the pre-edge at ~7113 eV of H-Fe-N_x-C was located close to those of Fe_2O_3 and FeTpp, indicating that a Fe^{2+}/Fe^{3+} mixture was present in the catalyst. Extended X-ray absorption fine structure (EXAFS) analysis enabled further probing of the Fe coordination environment. The EXAFS spectra in R space for H-Fe-N_x-C showed similar oscillations to the FeTpp reference, suggesting a uniform distribution of atomic Fe-N_4 sites throughout the hollow capsules (Fig. 3d). Unlike the reference iron foil, which showed a prominent Fe-Fe peak at 2.2 Å, H-Fe-N_x-C showed only a main peak at 1.51 Å in R space, close to the Fe-N peak of FeTpp and consistent with a Fe-N_x(C) scattering path. The fitting results gave an Fe coordination number of 4.2, consistent with a possible structure of Fe-N_4 with an Fe-N bond length of 2.02 Å (Figs. 3e and S20, and Table S2). As shown in the calculation model, these Fe-N_4 moieties were integrated in graphite-like planes (Fig. S21). The Mössbauer spectrum of H-Fe-N_x-C further revealed the presence of square-planar FeN_4 moieties, which were fitted using D_1 and D_3 doublets due to Fe(II) in medium and low spin states, and a D_2 doublet due to Fe(III) in a high spin state (Fig. 3f) [45–47]. These results were consistent with the Fe K-edge XANES results.

N_2 adsorption–desorption isotherms were collected at 77 K, from which the BET surface area of H-Fe-N_x-C was calculated to be 698.7 m^2 g^{-1} (Fig. S22, Table S1). The pore size distribution was calculated from the experimental isotherms using a density functional theory (DFT) model, confirming a hierarchical pore structure with the void diameters

clustered around 2.4–4.5 nm (Fig. S23). The high surface area and small size of the pore apertures were expected to be beneficial for ORR electrocatalysis, which was verified experimentally, as described below.

2.3. Electrocatalytic oxygen reduction reaction tests

H-Fe-N_x-C presents many desirable characteristics as an ORR catalyst. It supports well-dispersed iron single-atom sites in a hierarchically hollow porous conductive matrix, thereby allowing rapid mass transfer of reactants to active sites. A high nitrogen doping content also reduces the hydrophobicity of the carbon material, whilst a high pyridinic nitrogen content (and numerous Fe-N_x sites) will boost ORR electrocatalysis [48–51].

In this light, we anticipated excellent ORR activity from H-Fe-N_x-C in alkaline and acidic media. First, the catalytic properties of H-Fe-N_x-C for the ORR were evaluated in 0.1 M KOH, alongside a commercial Pt/C (20 wt% Pt) catalyst and metal-free hollow N-doped carbon capsules (HNCC). Detailed synthetic procedures and characterization data for HNCC are provided in the materials and methods section and supplementary materials (Figs. S4, S14–16, S18, S19, S24, S25, and Table S1). Linear sweep voltammetry (LSV) polarization curves for the different catalysts are presented in Fig. 4a. H-Fe-N_x-C afforded a positive ORR onset potential (E_{onset}) of ~1.05 V (vs. RHE). Remarkably, H-Fe-N_x-C achieved a half-wave potential ($E_{1/2}$) of 0.92 V, which exceeded that of commercial Pt/C (0.91 V) by 10 mV. Subsequently, LSV curves were measured at different rotation rates (Fig. 4b). The corresponding Koutecky–Levich (K-L) plots collected at non-Faradaic potentials ranging from 0.3 to 0.7 V are shown in Fig. 4c. The electron transfer number calculated for H-Fe-N_x-C was 3.7, confirming high selectivity for the four-electron oxygen reduction pathway ($O_2 + 2H_2O + 4e^- \rightarrow 4OH^-$). HNCC, the naked catalyst without the iron sites, showed much lower electrocatalytic activity (Fig. 4a) (see Fig. 5).

Good durability is vital for practical ORR catalysts. ORR chronoamperometric tests were performed at a potential of 0.664 V vs. RHE and a rotation speed of 900 rpm (Fig. 4d). H-Fe-N_x-C showed a stable ORR current–time profile over 6 h (Fig. 4d). Moreover, its stability was confirmed over 5000 test cycles with negligible loss of performance (only a slight decrease in the current density), indicating outstanding durability (Fig. 4e). Further, we subsequently examined the methanol tolerance (to assess the fuel crossover effect of H-Fe-N_x-C) by injecting methanol into the KOH solution during the chronoamperometric test. Fig. 4f shows that the current density for H-Fe-N_x-C was retained after 0.5 M or 6 M methanol was injected into the KOH solution. In contrast, the cathodic oxygen reduction peak for commercial Pt/C immediately vanished after methanol introduction. These results confirm that H-Fe-N_x-C has outstanding tolerance to methanol. Our large-scale synthesized

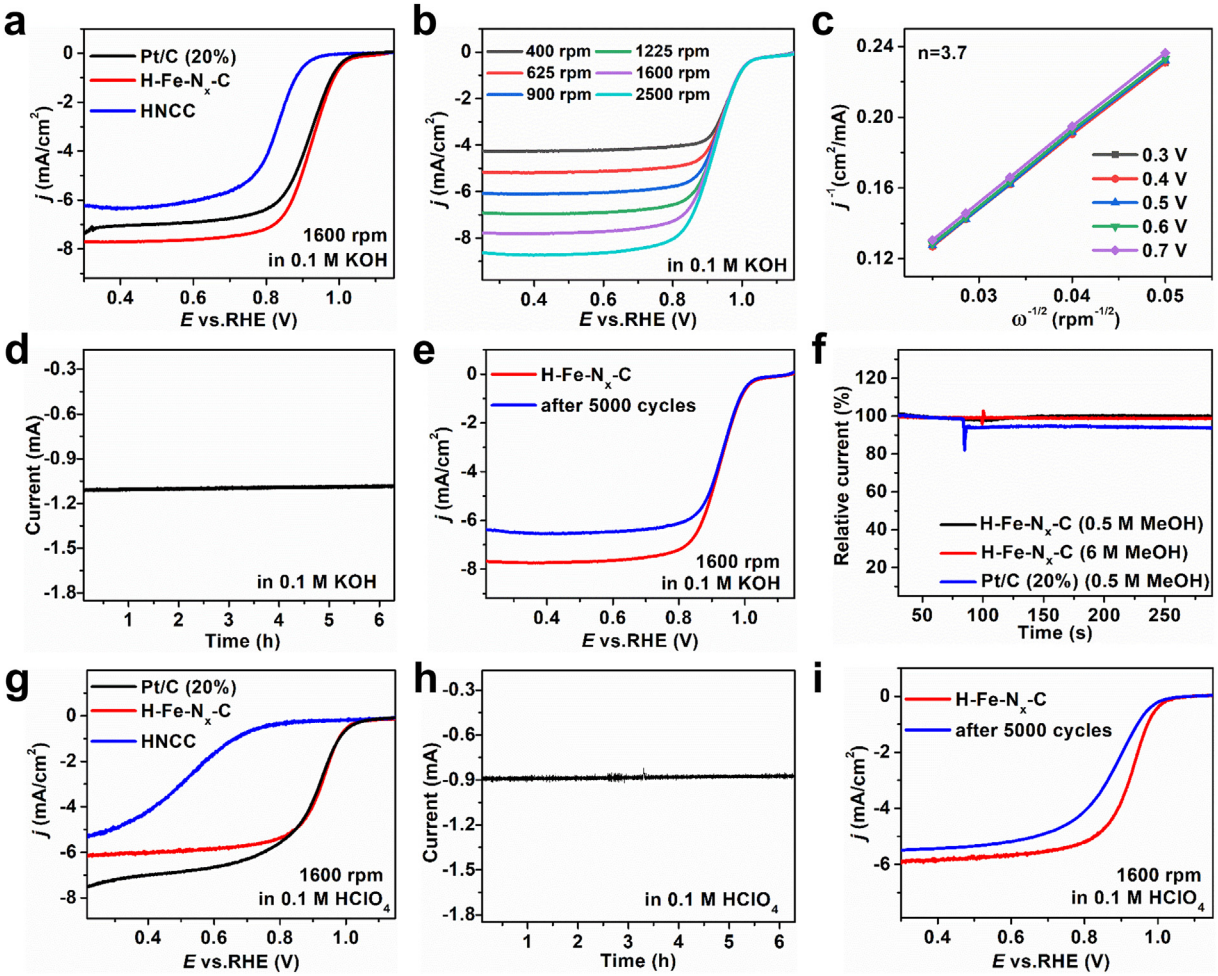

Fig. 4. ORR tests. (**a**) ORR polarization curves in 0.1 M KOH. (**b**) ORR polarization curves of H-Fe-N_x-C at different rotation rates. (**c**) Corresponding K–L plots of H-Fe-N_x-C, derived from RDE at different potentials. (**d**) Chronoamperometry i–t curve for H-Fe-N_x-C at a potential of 0.664 V in 0.1 M KOH. (**e**) ORR polarization curves before and after 5000 potential cycles in 0.1 M KOH. (**f**) Stability evaluation of H-Fe-N_x-C and Pt/C in O_2-saturated 0.1 M KOH with the injection of methanol. (**g**) ORR polarization curves in 0.1 M $HClO_4$. (**h**) Chronoamperometry i–t curve for H-Fe-N_x-C at a potential of 0.456 V in 0.1 M $HClO_4$. (**i**) ORR polarization curves before and after 5000 potential cycles in 0.1 M $HClO_4$. An iR correction was applied to all LSV curves.

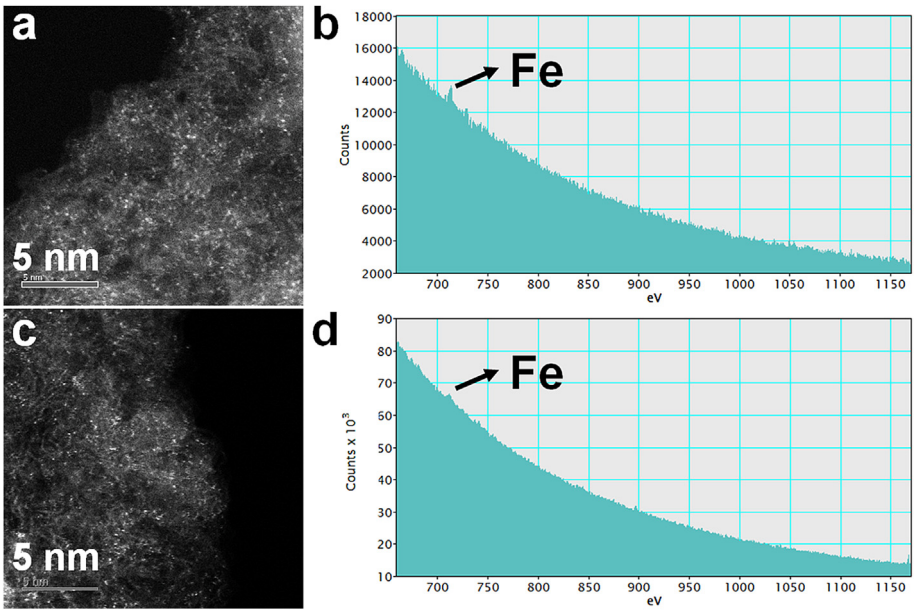

Fig. 5. Structural characterization after ORR tests. (a–b) Atomic-resolution HAADF-STEM image and Fe L-edge EELS spectrum for H-Fe-N_x-C after durability tests in 0.1 M KOH. (c–d) Atomic-resolution HAADF-STEM image and Fe L-edge EELS spectrum for H-Fe-N_x-C after durability tests in 0.1 M $HClO_4$.

H-Fe-N_x-C exhibited superior/comparable performance to most other state-of-the-art Fe-N-C catalysts (Table S3), thus offering great promise for practical applications.

The ORR performances of the materials were further evaluated in 0.1 M $HClO_4$. LSV experiments revealed the $E_{1/2}$ (vs. RHE) of H-Fe-N_x-C and commercial Pt/C (20 wt% Pt) to be 0.92 V and 0.90 V, respectively (Fig. 4g). Rotating ring disk electrode (RRDE) measurements were used to calculate an electron transfer number of ~4, indicating a four-electron transfer process (Fig. S26). ORR chronoamperometric tests further verified the good stability of the H-Fe-N_x-C after 6 h of running (Fig. 4h). However, decreases in $E_{1/2}$ (~40 mV) and current density (~0.42 mA cm^{-2}) were observed after 5000 continuous cycles in 0.1 M $HClO_4$ (Fig. 4i). Therefore, it is necessary to improve the material's stability in acidic media before it can be used in real applications.

We then carried out cyclic voltammetry (CV) tests and calculated the double-layer capacitance of the materials to determine the electrochemically active surface areas. The double-layer capacitance (C_{dl}) of H-Fe-N_x-C reached as high as 62.84 mF cm^{-2} in 0.1 M KOH and 63.29 mF cm^{-2} in 0.1 M $HClO_4$ (Figs. S27 and S28). The magnitude of C_{dl} was proportional to the electroactive surface area. Next, LSVs were measured in N_2-saturated 0.1 M KOH solution (and 0.1 M $HClO_4$ solution) at 1600 rpm (Figs. S29 and S30). The results revealed that the catalysts themselves were responsible for the high current densities realized during the ORR processes. In addition, the adsorption of oxygen by porous carbon might have changed the limiting diffusion current densities in the reactions. Taken together, these results explain the superior electrocatalytic activity of the H-Fe-N_x-C sample. With respect to the structure of H-Fe-N_x-C after being used as an ORR catalyst, atomic-resolution HAADF-STEM as well as Fe L-edge and N K-edge electron energy loss spectra (EELS) showed that the atomically dispersed FeN_x sites were maintained (Figs. 5, S31 and S32). We estimated the cost of synthesizing H-Fe-N_x-C to be appropriately 215.2 CNY/g (~33.8 USD/g) (Table S4), far cheaper than commercial Pt/C (20 wt% Pt, ~108.3 USD/g), suggesting the catalyst's economic feasibility.

3. Discussion

Considering the data above, it is evident that our large-scale synthetic methodology for H-Fe-N_x-C, employing a precursor comprised of metal/tannic acid polymer shells on ZIF-8 nanocrystals, delivers a hollow iron-nitrogen-doped carbon catalyst with outstanding ORR performance. Based on a raft of complementary experimental analyses, we demonstrated that H-Fe-N_x-C presents a hollow capsule architecture containing atomically dispersed FeN_4 porphyrin-like sites, a high level of nitrogen dopant, a hierarchical micropore/mesopore structure, and a high surface area. Benefiting from these rich attributes, H-Fe-N_x-C demonstrated state-of-the-art ORR performance for a Fe-N-C catalyst in alkaline media. Importantly, the same synthetic approach could easily be adopted for the large-scale synthesis of other M-N-C catalysts with highly dispersed metal single sites.

4. Conclusions

In summary, we have reported a large-scale synthetic method for hollow and microporous/mesoporous nitrogen-doped carbon capsules functionalized with single-atom iron (FeN_4) moieties in the walls. The FeN_4 sites were embedded in the basal planes of graphite domains. Benefiting from its open porous structure and the accessibility of the FeN_4 sites, H-Fe-N_x-C demonstrated excellent ORR activity and long-term stability, surpassing most state-of-the-art single-atom catalysts and a commercial Pt/C benchmark catalyst. Our results indicate a practical route to achieving a diverse array of porous M-N-C materials for oxygen electrocatalysis and other catalytic applications.

5. Materials and methods

Synthesis of ZIF-8@K-TA core–shell nanocrystals. For the synthesis of ZIF-8@K-TA core–shell nanocrystals, our previous method was used, with a slight modification [39,41]. Specifically, 50 g of ZIF-8 nanocrystals were dispersed in 2.5 L of deionized water by sonication for 10 min. At this stage, a 24 mM tannic acid solution (600 mL) was prepared, and the pH was adjusted to ~8 using a 6 M KOH solution. After that, the tannic acid solution and ZIF-8 suspension were mixed. The obtained suspension was stirred for 10 min, after which the solid was collected by centrifugation, washed with methanol, then dried under vacuum to yield ZIF-8@K-TA.

Synthesis of ZIF-8@Fe-TA core–shell nanocrystals. ZIF-8@Fe-TA core–shell nanocrystals were initially prepared according to our previous general method, with a slight modification [39,41]. The obtained ZIF-8@K-TA were ultrasonically dispersed in 4.3 L of methanol

containing 2 g of $Fe(NO_3)_3{\cdot}9H_2O$ for 5 min, forming a uniform suspension. Subsequently, the suspension was continuously stirred for 2 h. Afterwards, the solid product (ZIF-8@Fe-TA) was isolated by centrifugation, washed with methanol, and finally dried under vacuum.

Synthesis of H-Fe-N_x-C and HNCC. The obtained ZIF-8@Fe-TA was pyrolyzed by heat treatment at 900 °C for 3 h under an Ar atmosphere (1 °C/min to 900 °C). The obtained product was leached in 3 M HCl at 85 °C for 24 h, then washed with deionized water and dried under vacuum. Subsequently, the black powder was heated at 900 °C (under an Ar flow) for another 3 h to acquire the final H-Fe-N_x-C product. For the preparation of HNCC, a similar method was used, except that ZIF-8@Fe-TA was replaced by ZIF-8@K-TA.

Electrochemical measurements. All the electrochemical measurements reported in this work used a conventional three-electrode system on a CHI660E electrochemical station. A Pine Instruments MSR rotator and rotating disk electrode (RDE) with a glassy carbon disk (or rotating ring disk electrode, RRDE) were used as the substrate for the working electrode. Ag/AgCl (3.5 M KCl solution) and a platinum wire were used as the reference and counter electrodes, respectively. Catalyst inks were prepared by dispersing 5 mg of the catalyst in a mixture of ethanol (1 mL) and Nafion solution (100 μL). The ink was ultrasonically mixed for 30 min and continually stirred during the electrode fabrication step. 10 μL of the catalyst ink was deposited onto the glassy carbon disk (area 0.19625 cm^2 for the RDE and 0.2475 cm^2 for the RRDE), then the modified electrode was dried in air. Linear sweep voltammetry (LSV) and cyclic voltammetry (CV) data were measured in an O_2 (or N_2)-saturated 0.1 M KOH solution (or a 0.1 M $HClO_4$ solution). The electrolyte was purged with oxygen (or nitrogen) for 40 min before starting the tests, and purging was continuous during the tests. All current densities reported in this work were calculated based on the geometrical area of a rotating disk electrode. The numbers of electrons transferred (n) during the ORR at various electrode potentials were calculated using the Koutecky–Levich equation:

$$\frac{1}{j}=\frac{1}{j_L}+\frac{1}{j_K}=\frac{1}{B\omega^{1/2}}+\frac{1}{j_K}$$

$$B=0.62nFC_0D_0^{2/3}\nu^{-1/6}$$

where j is the measured current density; j_K and j_L are the kinetic and diffusion-limiting current densities, respectively; ω is the angular velocity of the disk ($\omega = 2\pi N$, N being the linear rotation speed); n represents the overall number of electrons transferred in the oxygen reduction reaction; F is the Faraday constant; C_0 is the bulk concentration of O_2 (1.2×10^{-6} mol cm^{-3}); D_0 is the diffusion coefficient of O_2 in 0.1 M KOH electrolyte (1.9×10^{-5} cm^2 s^{-1}); ν is the kinematics viscosity of the electrolyte, and k is the electron-transfer rate constant.

The RRDE measurements were performed in 0.1 M $HClO_4$ solution. The peroxide yields (H_2O_2%) were calculated from the ring current (I_r) and the disk current (I_d) using the equation:

$$H_2O_2(\%)=200\times\frac{\frac{I_r}{N}}{I_d+\frac{I_r}{N}}$$

The electron transfer number (n) in acid was calculated using the equation:

$$n=4\times\frac{I_d}{\frac{I_r}{N}+I_d}$$

where $N = 0.42$ is the current collection efficiency of the Pt ring.

Author contributions

H. Yang, S. G. Telfer, P. E. Kruger, and S. Ma conceived the research. H. Yang, Y. Liu, and X. Liu carried out the synthetic chemistry. H. Yang, Y. Liu, and X. Liu performed most of the material characterizations. H. Tian analyzed the atomic resolution HAADF-STEM characterizations. H. Yang, X. Liu, and G. I. N. Waterhouse performed the XAS and XPS characterizations. H. Yang, X. Liu, and Y. Liu performed the electrochemical measurements. H. Yang, X. Wang, G. I. N. Waterhouse, P. E. Kruger, S. G. Telfer, and S. Ma wrote the manuscript. All authors contributed to discussions.

Additional information

Chemicals, instrumentation, experimental methods, and additional materials characterization (FTIR, powder X-ray diffraction, SEM, EDS, TEM, Raman, gas sorption analysis, pore size distribution calculations, XPS, XAS, EELS, electrochemical results, and calculations) are included in the Supplementary Material.

Competing financial interests

The authors declare no competing financial interests.

Declaration of competing interest

The authors declare that they have no known competing financial interests or personal relationships that could have appeared to influence the work reported in this paper.

Acknowledgments

We gratefully acknowledge funding support from the Robert A. Welch Foundation (B−0027) (SM), National Science Foundation of China (Grants 22006036), North China Electric Power University (XM2112307) (HY and XW). GINW is supported by a James Cook Research Fellowship from New Zealand Government funding, administered by the Royal Society Te Apārangi. We also acknowledge support from the XAS beamline scientists of the Australian Synchrotron and the 14 W station of the Shanghai Synchrotron Radiation Facility (SSRF).

Appendix A. Supplementary data

Supplementary data to this article can be found online at https://doi.org/10.1016/j.esci.2022.02.005.

References

[1] H.-F. Wang, Q. Xu, Materials design for rechargeable metal-air batteries, Matter 1 (2019) 565–595.
[2] X. Zhang, X.-G. Wang, Z. Xie, Z. Zhou, Recent progress in rechargeable alkali metal–air batteries, Green Energy Environ. 1 (2016) 4–17.
[3] D.R. Dekel, Review of cell performance in anion exchange membrane fuel cells, J. Power Sources 375 (2018) 158–169.
[4] G. Merle, M. Wessling, K. Nijmeijer, Anion exchange membranes for alkaline fuel cells: a review, J. Membr. Sci. 377 (2011) 1–35.
[5] Q.Q. Zhang, J.Q. Guan, Single-atom catalysts for electrocatalytic applications, Adv. Funct. Mater. 30 (2020) 2000768.
[6] Z.-F. Huang, J. Wang, Y. Peng, C.-Y. Jung, A. Fisher, X. Wang, Design of efficient bifunctional oxygen reduction/evolution electrocatalyst: recent advances and perspectives, Adv. Energy Mater. 7 (2017) 1700544.
[7] X. Ge, A. Sumboja, D. Wuu, T. An, B. Li, F.W.T. Goh, T.S.A. Hor, Y. Zong, Z. Liu, Oxygen reduction in alkaline media: from mechanisms to recent advances of catalysts, ACS Catal. 5 (2015) 4643–4667.
[8] N. Zhang, L. Li, Y. Chu, L. Zheng, S. Sun, G. Zhang, H. He, J. Zhao, High Pt utilization efficiency of electrocatalysts for oxygen reduction reaction in alkaline media, Catal. Today 332 (2019) 101–108.
[9] X. Ren, Q. Lv, L. Liu, B. Liu, Y. Wang, A. Liu, G. Wu, Current progress of Pt and Pt-based electrocatalysts used for fuel cells, Sustain, Energy Fuels 4 (2020) 15–30.
[10] Y. Wang, J. Li, Z. Wei, Transition-metal-oxide-based catalysts for the oxygen reduction reaction, J. Mater. Chem. 6 (2018) 8194–8209.
[11] H. Zhu, S. Zhang, Y.X. Huang, L. Wu, S. Sun, Monodisperse $M_xFe_{3-x}O_4$ (M = Fe, Cu, Co, Mn) nanoparticles and their electrocatalysis for oxygen reduction reaction, Nano Lett. 13 (2013) 2947–2951.

[12] H. Osgood, S.V. Devaguptapu, H. Xu, J. Cho, G. Wu, Transition metal (Fe, Co, Ni, and Mn) oxides for oxygen reduction and evolution bifunctional catalysts in alkaline media, Nano Today 11 (2016) 601–625.
[13] K. Chen, X. Huang, C. Wan, H. Liu, Hybrids based on transition metal phosphide (Mn_2P, Co_2P, Ni_2P) nanoparticles and heteroatom-doped carbon nanotubes for efficient oxygen reduction reaction, RSC Adv. 5 (2015) 92893–92898.
[14] F. Bai, H. Huang, C. Hou, P. Zhang, Porous carbon-coated cobalt sulfide nanocomposites derived from metal organic frameworks (MOFs) as an advanced oxygen reduction electrocatalyst, New J. Chem. 40 (2016) 1679–1684.
[15] S. Zhao, H. Yin, L. Du, L. He, K. Zhao, L. Chang, G. Yin, H. Zhao, S. Liu, Z. Tang, Carbonized nanoscale metal-organic frameworks as high performance electrocatalyst for oxygen reduction reaction, ACS Nano 8 (2014) 12660–12668.
[16] X. Qiao, J. Jin, H. Fan, Y. Li, S. Liao, In situ growth of cobalt sulfide hollow nanospheres embedded in nitrogen and sulfur co-doped graphene nanoholes as a highly active electrocatalyst for oxygen reduction and evolution, J. Mater. Chem. 5 (2017) 12354–12360.
[17] C. Wan, X. Duan, Y. Huang, Molecular Design of single-atom catalysts for oxygen reduction reaction, Adv. Energy Mater. 10 (2020) 1903815.
[18] L. Peng, L. Shang, T. Zhang, G.I.N. Waterhouse, Recent advances in the development of single-atom catalysts for oxygen electrocatalysis and zinc–air batteries, Adv. Energy Mater. 10 (2020) 2003018.
[19] Q. Wang, Y. Yang, F. Sun, G. Chen, J. Wang, L. Peng, W.-T. Chen, L. Shang, J. Zhao, D. Sun-Waterhouse, T. Zhang, G.I.N. Waterhouse, Molten NaCl-assisted synthesis of porous Fe-N-C electrocatalysts with a high density of catalytically accessible FeN_4 active sites and outstanding oxygen reduction reaction performance, Adv. Energy Mater. 11 (2021) 2100219.
[20] Q. He, Y. Meng, H. Zhang, Y. Zhang, H. Chen, H. Xiao, X. He, M. Wu, H. Ji, Facile synthesis of impurity-free iron single atom catalysts for highly efficient oxygen reduction reaction and active-site identification, Catal. Sci. Technol. 9 (2019) 6556–6560.
[21] J. Han, H. Bao, J.-Q. Wang, L. Zheng, S. Sun, Z.L. Wang, C. Sun, 3D N-doped ordered mesoporous carbon supported single-atom Fe-N-C catalysts with superior performance for oxygen reduction reaction and zinc-air battery, Appl. Catal. B 280 (2021) 119411.
[22] Y. Chen, S. Ji, Y. Wang, J. Dong, W. Chen, Z. Li, R. Shen, L. Zheng, Z. Zhuang, D. Wang, Y. Li, Isolated single iron atoms anchored on N-doped porous carbon as an efficient electrocatalyst for the oxygen reduction reaction, Angew. Chem. Int. Ed. 56 (2017) 6937–6941.
[23] X. Zhang, S. Zhang, Y. Yang, L. Wang, Z. Mu, H. Zhu, X. Zhu, H. Xing, H. Xia, B. Huang, J. Li, S. Guo, E. Wang, A general method for transition metal single atoms anchored on honeycomb-like nitrogen-doped carbon nanosheets, Adv. Mater. 32 (2020) 1906905.
[24] G. Chen, P. Liu, Z. Liao, F. Sun, Y. He, H. Zhong, T. Zhang, E. Zschech, M. Chen, G. Wu, J. Zhang, X. Feng, Zinc-mediated template synthesis of Fe-N-C electrocatalysts with densely accessible Fe-N_x active sites for efficient oxygen reduction, Adv. Mater. 32 (2020) 1907399.
[25] L. Lin, Q. Zhu, A.W. Xu, Noble-metal-free Fe-N/C catalyst for highly efficient oxygen reduction reaction under both alkaline and acidic conditions, J. Am. Chem. Soc. 136 (2014) 11027–11033.
[26] J. Ding, P. Wang, S. Ji, H. Wang, V. Linkov, R. Wang, N-doped mesoporous FeN_x/carbon as ORR and OER bifunctional electrocatalyst for rechargeable zinc-air batteries, Electrochim. Acta 296 (2019) 653–661.
[27] X. Wan, X. Liu, Y. Li, R. Yu, L. Zheng, W. Yan, H. Wang, M. Xu, J. Shui, Fe–N–C electrocatalyst with dense active sites and efficient mass transport for high-performance proton exchange membrane fuel cells, Nat. Catal. 2 (2019) 259–268.
[28] Y.-Z. Chen, C. Wang, Z.-Y. Wu, Y. Xiong, Q. Xu, S.-H. Yu, H.-L. Jiang, From bimetallic metal-organic framework to porous carbon: high surface area and multicomponent active dopants for excellent electrocatalysis, Adv. Mater. 27 (2015) 5010–5016.
[29] P. Yin, T. Yao, Y. Wu, L. Zheng, Y. Lin, W. Liu, H. Ju, J. Zhu, X. Hong, Z. Deng, G. Zhou, S. Wei, Y. Li, Single cobalt atoms with precise N-coordination as superior oxygen reduction reaction catalysts, Angew. Chem. Int. Ed. 55 (2016) 10800–10805.
[30] C. Zhu, Q. Shi, B.Z. Xu, S. Fu, G. Wan, C. Yang, S. Yao, J. Song, H. Zhou, D. Du, S.P. Beckman, D. Su, Y. Lin, Hierarchically porous M–N–C (M = Co and Fe) single-atom electrocatalysts with robust MN_x active moieties enable enhanced ORR performance, Adv. Energy Mater. 8 (2018) 1801956.
[31] L. Shang, H. Yu, X. Huang, T. Bian, R. Shi, Y. Zhao, G.I.N. Waterhouse, L.-Z. Wu, C.-H. Tung, T. Zhang, Well-dispersed ZIF-derived Co,N-Co-doped carbon nanoframes through mesoporous-silica-protected calcination as efficient oxygen reduction electrocatalysts, Adv. Mater. 28 (2016) 1668–1674.
[32] T. Sun, Y. Li, T. Cui, L. Xu, Y.-G. Wang, W. Chen, P. Zhang, T. Zheng, X. Fu, S. Zhang, Z. Zhang, D. Wang, Y. Li, Engineering of coordination environment and multiscale structure in single-site copper catalyst for superior electrocatalytic oxygen reduction, Nano Lett. 20 (2020) 6206–6214.
[33] G. Han, Y. Zheng, X. Zhang, Z. Wang, Y. Gong, C. Du, M.N. Banis, Y.-M. Yiu, T.-K. Sham, L. Gu, Y. Sun, Y. Wang, J. Wang, Y. Gao, G. Yin, X. Sun, High loading single-atom Cu dispersed on graphene for efficient oxygen reduction reaction, Nano Energy 66 (2019) 104088.
[34] Q. Zhou, J. Cai, Z. Zhang, R. Gao, B. Chen, G. Wen, L. Zhao, Y. Deng, H. Dou, X. Gong, Y. Zhang, Y. Hu, A. Yu, X. Sui, Z. Wang, Z. Chen, A gas-phase migration strategy to synthesize atomically dispersed Mn-N-C catalysts for Zn–Air batteries, Small Methods 5 (2021) 2100024.
[35] H.-Y. Kim, Y.-W. Ju, Fabrication of Mn-N-C catalyst for oxygen reduction reactions using Mn-embedded carbon nanofiber, Energies 13 (2020) 2561.
[36] Y. Wang, X. Zhang, S. Xi, X. Xiang, Y. Du, P. Chen, D. Lyu, S. Wang, Z.Q. Tian, P.K. Shen, Rational design and synthesis of hierarchical porous Mn–N–C nanoparticles with atomically dispersed MnN_x moieties for highly efficient oxygen reduction reaction, ACS Sustain. Chem. Eng. 8 (2020) 9367–9376.
[37] X. Wei, D. Zheng, M. Zhao, H. Chen, X. Fan, B. Gao, L. Gu, Y. Guo, J. Qin, J. Wei, Y. Zhao, G. Zhang, Cross-linked polyphosphazene hollow nanosphere-derived N/P-doped porous carbon with single nonprecious metal atoms for the oxygen reduction reaction, Angew. Chem. Int. Ed. 59 (2020) 14639–14646.
[38] D. Geng, Y. Chen, Y. Chen, Y. Li, R. Li, X. Sun, S. Ye, S. Knights, High oxygen-reduction activity and durability of nitrogen-doped graphene, Energy Environ. Sci. 4 (2011) 760–764.
[39] H. Yang, S.J. Bradley, A. Chan, G.I.N. Waterhouse, T. Nann, P.E. Kruger, S.G. Telfer, Catalytically active bimetallic nanoparticles supported on porous carbon capsules derived from metal-organic framework composites, J. Am. Chem. Soc. 138 (2016) 11872–11881.
[40] H. Yang, S.J. Bradley, X. Wu, A. Chan, G.I.N. Waterhouse, T. Nann, J. Zhang, P.E. Kruger, S. Ma, S.G. Telfer, General synthetic strategy for libraries of supported multicomponent metal nanoparticles, ACS Nano 12 (2018) 4594–4604.
[41] H. Yang, X. Chen, W.T. Chen, Q. Wang, N.C. Cuello, A. Nafady, A.M. Al-Enizi, G.I.N. Waterhouse, G.A. Goenaga, T.A. Zawodzinski, T. Nann, P.E. Kruger, J.E. Clements, J. Zhang, H. Tian, S.G. Telfer, S. Ma, Tunable synthesis of hollow metal-nitrogen-carbon capsules for efficient oxygen reduction catalysis in proton exchange membrane fuel cells, ACS Nano 13 (2019) 8087–8098.
[42] H. Yang, X. Liu, M. Hao, Y. Xie, X. Wang, H. Tian, G.I.N. Waterhouse, P.E. Kruger, S.G. Telfer, S. Ma, Functionalized iron-nitrogen-carbon electrocatalyst provides a reversible electron transfer platform for efficient uranium extraction from seawater, Adv. Mater. (2021) 2106621.
[43] H. Yang, X. Wang, T. Zheng, N.C. Cuello, G. Goenaga, T.A. Zawodzinski, H. Tian, J.T. Wright, R.W. Meulenberg, X. Wang, Z. Xia, S. Ma, CrN-encapsulated hollow Cr-N-C capsules boosting oxygen reduction catalysis in PEMFC, CCS Chem. 3 (2021) 208–218.
[44] H. Zhang, S. Hwang, M. Wang, Z. Feng, S. Karakalos, L. Luo, Z. Qiao, X. Xie, C. Wang, D. Su, Y. Shao, G. Wu, Single atomic iron catalysts for oxygen reduction in acidic media: particle size control and thermal activation, J. Am. Chem. Soc. 139 (2017) 14143–14149.
[45] Z. Miao, X. Wang, Z. Zhao, W. Zuo, S. Chen, Z. Li, Y. He, J. Liang, F. Ma, H.-L. Wang, G. Lu, Y. Huang, G. Wu, Q. Li, Improving the stability of non-noble-metal M-N-C catalysts for proton-exchange-membrane fuel cells through M-N bond length and coordination regulation, Adv. Mater. 33 (2021) 2006613.
[46] L. Jiao, J. Li, L.L. Richard, Q. Sun, T. Stracensky, E. Liu, M.T. Sougrati, Z. Zhao, F. Yang, S. Zhong, H. Xu, S. Mukerjee, Y. Huang, D.A. Cullen, J.H. Park, M. Ferrandon, D.J. Myers, F. Jaouen, Q. Jia, Chemical vapour deposition of Fe-N-C oxygen reduction catalysts with full utilization of dense Fe-N_4 sites, Nat. Mater. 20 (2021) 1385–1391.
[47] D. Menga, J.L. Low, Y.S. Li, I. Arcon, B. Koyuturk, F. Wagner, F. Ruiz-Zepeda, M. Gaberšček, B. Paulus, T.-P. Paulus, Resolving the dilemma of Fe-N-C catalysts by the selective synthesis of tetrapyrrolic active sites via an imprinting strategy, J. Am. Chem. Soc. 143 (2021) 18010–18019.
[48] X. Ning, Y. Li, J. Ming, Q. Wang, H. Wang, Y. Cao, F. Peng, Y. Yang, H. Yu, Electronic synergism of pyridinic- and graphitic-nitrogen on N-doped carbons for the oxygen reduction reaction, Chem. Sci. 10 (2019) 1589–1596.
[49] K.V. Kumar, K. Preuss, Z.X. Guo, M.M. Titirici, Understanding the hydrophilicity and water adsorption behavior of nanoporous nitrogen-doped carbons, J. Phys. Chem. C 120 (2016) 18167–18179.
[50] L. Liu, G. Zeng, J. Chen, L. Bi, L. Dai, Z. Wen, N-doped porous carbon nanosheets as pH-universal ORR electrocatalyst in various fuel cell devices, Nano Energy 49 (2018) 393–402.
[51] Y. Zhao, J. Wan, H. Yao, L. Zhang, K. Lin, L. Wang, N. Yang, D. Liu, L. Song, J. Zhu, L. Gu, L. Liu, H. Zhao, Y. Li, D. Wang, Few-layer graphdiyne doped with sp-hybridized nitrogen atoms at acetylenic sites for oxygen reduction electrocatalysis, Nat. Chem. 10 (2018) 924–931.